Journal of the Mechanics and Physics of Solids 96 (2016) 312–332

Contents lists available at ScienceDirect

Journal of the Mechanics and Physics of Solids

journal homepage: www.elsevier.com/locate/jmps

Dynamics of crack penetration vs. branching at a weak interface: An experimental study

Balamurugan M. Sundaram, Hareesh V. Tippur *,[1]

Department of Mechanical Engineering, Auburn University, AL 36849, United States

ARTICLE INFO

Article history:
Received 31 March 2016
Received in revised form
9 July 2016
Accepted 28 July 2016
Available online 29 July 2016

Keywords:
Dynamic fracture
Crack-interface interaction
Crack branching
Mixed-mode fracture
Digital gradient sensing
Transparent materials

ABSTRACT

In this paper, the dynamic crack-interface interactions and the related mechanics of crack penetration vs. branching at a weak interface are studied experimentally. The interface is oriented perpendicular to the incoming mode-I crack in an otherwise homogeneous bilayer. The focus of this investigation is on the effect of interface location and the associated crack-tip parameters within the bilayer on the mechanics of the ensuing fracture behavior based on the optical methodologies laid down in Ref. Sundaram and Tippur (2016). Time-resolved optical measurement of crack-tip deformations, velocity and stress intensity factor histories in different bilayer configurations is performed using Digital Gradient Sensing (DGS) technique in conjunction with high-speed photography. The results show that the crack path selection at the interface and subsequently the second layer are greatly affected by the location of the interface within the geometry. Using optically measured fracture parameters, the mechanics of crack penetration and branching are explained. Counter to the intuition, a dynamically growing mode-I crack approaching a weak interface at a lower velocity and stress intensity factor penetrates the interface whereas a higher velocity and stress intensity factor counterpart gets trapped by the interface producing branched daughter cracks until they kink out into the next layer. An interesting empirical observation based on measured crack-tip parameters for crack penetration and branching is also made.

1. Introduction

The competition between crack penetration, deflection, and branching behaviors at interfaces govern the fracture mechanics of brittle layered solids and structures. Early work by Cook and Gordon (1964) has suggested the possibility of strength and toughness enhancement of such systems by optimizing the ratio between the adhesive strength of the interface and the cohesive strength of the brittle phase. Several works reported since, most performed under quasi-static conditions (He and Hutchinson, 1989; Gupta et al., 1992; Leguillion et al., 2000; Paramgiani and Thouless, 2006; Xia et al., 2012), have studied various aspects of this problem. The dynamic counterparts of these introduce a host of additional parameters such as crack velocity, inertia, stress-wave interactions, making the problem more challenging.

Most reports on this topic that deal with dynamic interfacial crack growth *along an interface* (Tippur and Rosakis, 1991; Washabagh and Knauss, 1994) have brought to light several previously unknown aspects of fracture mechanics including unusually high crack speeds and the possibility of crack propagation at intersonic speeds (Lambros and Rosakis, 1995;

* Corresponding author.
E-mail address: tippuhv@auburn.edu (H.V. Tippur).
[1] McWane Professor.

http://dx.doi.org/10.1016/j.jmps.2016.07.020
0022-5096/

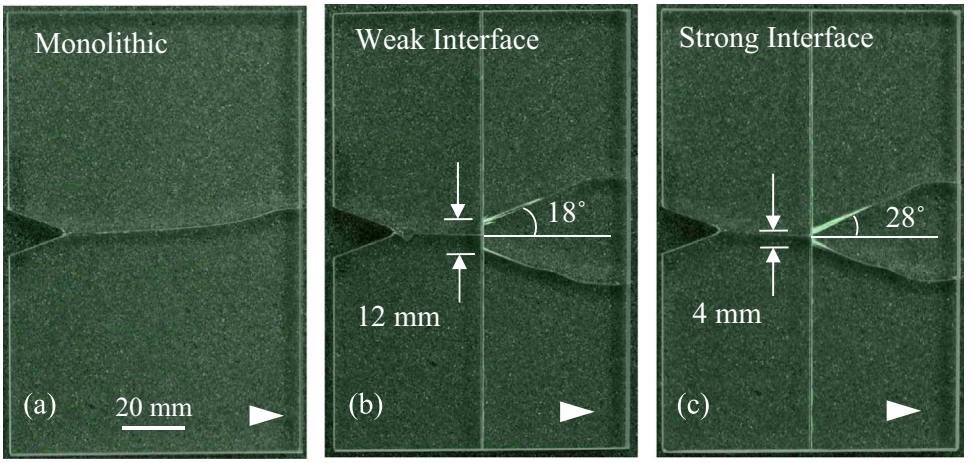

Fig. 1. Photographs of fractured specimens from the previous study showing crack path selection in (a) Monolithic (b) 'Weak' 90° layered configuration (c) 'Strong' 90° layered configuration. Arrowhead indicates crack growth direction (Sundaram and Tippur, 2016).

Rosakis et al., 1998; Coker and Rosakis, 2001). Further, to fully comprehend the dynamic fracture of layered materials, crack growth across interfaces needs to be understood as well. The existing studies on this subject generally deal with interfaces *inclined* to the crack propagation direction where deflection/penetration mechanics of a single crack tip are analyzed. Rosakis and his co-workers (Xu et al., 2003; Chalivendra and Rosakis, 2008) are among the few who have studied in detail interactions between a dynamically growing crack and an inclined interface experimentally. They have used optical methods to visualize crack-tip fields and location during highly transient fracture events. Understanding the mechanics of a dynamically growing crack becoming an interfacial crack when it encounters an interface is addressed in their works. They have observed significant jumps in crack velocity as well as crack deflection at an interface. Xu and Wang (Xu and Wang, 2006) have recently revisited those measurements and suggest that the *T*-stress could also play a significant role in the interfacial debond initiation besides stress intensity factors. Park and Chen (Park and Chen, 2011) have visualized fast-fracture in layered glass using high-speed photography. Specifically, they have examined crack branching and arrest behaviors at an interface as a function of interfacial characteristics such as thickness, strength, and surface finish.

A few numerical investigations using finite element analyses, either in conjunction with stiffness degradation techniques (Timmel et al., 2007) or using cohesive elements (Siegmund et al., 1997), and peridynamic simulations (Hu et al., 2013) have also been reported on crack growth across interfaces. The stiffness degradation or element erosion techniques usually suffer from mesh refinement issues. The analysis based on cohesive elements, on the other hand, are more common; for example, in Siegmund et al. (1997) the role of interface strength on crack penetration vs. deflection at an interface situated perpendicular to the crack growth direction using cohesive elements is examined. Higher strength of the interface is shown to promote crack penetration whereas the weaker one causes the crack to deflect at the interface. In a more recent study, Liu et al. (2011) have studied strain rate effects on growth dynamics of a crack-tip lodged into an interface perpendicular to the crack. The possibilities of crack growth through the interface as well as its bifurcation along the interface before entering the next layer are examined in their work.

In this context, *the research reported here exploits the experimental methodology demonstrated by the authors' in a previous report on dynamic crack growth in PMMA bilayers* (Sundaram and Tippur, 2016). Previously, the feasibility of a relatively new optical technique called Digital Gradient Sensing (DGS) technique for mapping crack-tip deformations when a mode-I crack branches at an interface oriented perpendicular to a growing crack was demonstrated. Unlike its monolithic counterpart where a single crack traversed the entire uncracked ligament *without branching*, in bilayers the dynamically growing mode-I *mother* crack in the first layer transitioned to an interfacial crack at the weak plane before penetrating the next layer as two globally symmetric but locally mixed-mode *daughter* cracks, as shown in Fig. 1. An increased fracture surface area and crack velocity perturbations[2] were caused by the interface situated in the crack path. The effect of two different interface fracture toughness, both weak relative to the parent material (approx. 75% and 50% of the crack initiation toughness of PMMA and identified as 'strong' and 'weak', respectively), were examined. A methodology for evaluating stress intensity factors of mixed-mode cracks using the DGS technique under dynamic conditions was also developed. Thus measured crack driving forces at the branched crack-tips were lower than the monolithic counterpart. Further, the weaker of the two interfaces was found to be a more favorable configuration in terms of energy absorption and crack arrest.

Building upon Sundaram and Tippur (2016), the *focus of this work* is to examine the conditions under which a dynamically propagating mode-I crack in the first layer of the bilayer would penetrate the interface with and without crack branching. The measurement of full-field crack-tip deformations, crack velocities and stress intensity factors (a) when a mode-I crack approaches the interface, and (b) when the crack departs from the interface into the second layer either as a single mode-I crack or multiple

[2] Crack branching in monolithic materials is known to occur with very little change in crack velocity (Freund, 1998).

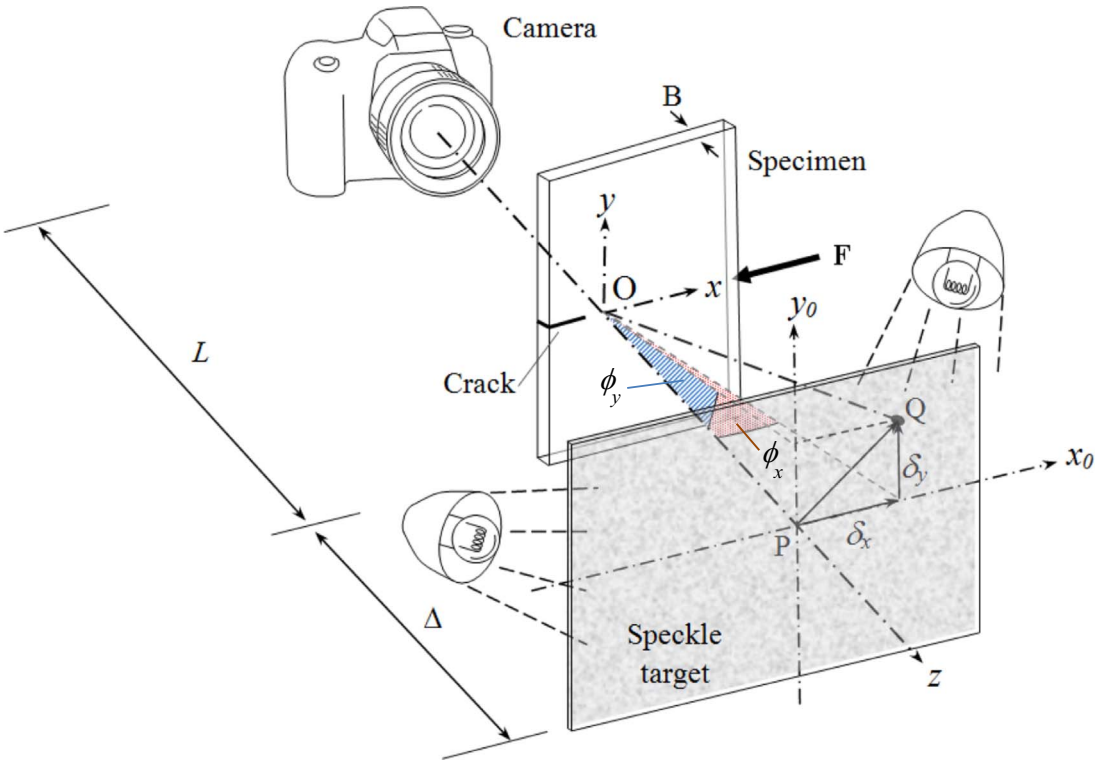

Fig. 2. The schematic of the experimental setup for transmission-mode. Digital Gradient Sensing (DGS) technique to determine planar stress gradients in phase objects.

mixed-mode cracks, are used to explain the underlying mechanics. In the following, after a brief description of the optical method, the specimen geometry and the experimental setup, the details of experimental results for different interface locations relative to the initial notch tip are presented. The measured crack-tip fields, crack length and velocity histories, and stress intensity factor histories are described next. Subsequently, using the prevailing dynamic crack-tip field descriptions, the stresses at the interface are evaluated as the crack approaches it. Thus evaluated stresses are used to explain the observations based on measured interface characteristics. An empirical observation based on measured fracture parameter histories is also put forward.

2. Digital gradient sensing (DGS)

A schematic of the experimental setup for transmission-mode DGS technique is shown in Fig. 2. In this technique (Periasamy and Tippur, 2013) a random speckle pattern on a planar surface, referred to as the target, is photographed through a planar, optically transparent object being studied. Ordinary white light illumination is used to record the gray scales on the target. The speckle pattern is first photographed through the specimen in its undeformed state to obtain a reference image. That is, a point P on the target plane (x_0–y_0 plane) is recorded by the camera through point O on the specimen plane (x–y plane). Upon loading, the non-uniform state of stress alters the refractive index of the specimen in the crack-tip vicinity. Additionally, the Poisson effect produces non-uniform thickness changes. A combination of these, known as the *elasto-optical effect*, causes the light rays to deflect from their original path as they propagate in the crack-tip vicinity. The speckle pattern is once again photographed through the specimen in the deformed state. Then a neighboring point Q on the target plane is recorded by the camera through point O on the specimen plane after deformation. The local deviations of light rays can be quantified by correlating speckle images in the deformed and reference states. Once displacements δ_x and δ_y are evaluated from digital image correlation, the angular deflections of light rays ϕ_x and ϕ_y in two orthogonal planes (x–z and y–z planes, the z-axis coinciding with the optical axis of the setup and x–y being the specimen plane coordinates) can be computed knowing the distance between the specimen plane and the target plane. A detailed analysis by Periasamy and Tippur (2013) shows that the local angular deflections are related to the gradients of the in-plane normal stresses as,

$$\phi_{x;y} = \pm C_\sigma B \frac{\partial(\sigma_x + \sigma_y)}{\partial x;\, y} = \pm C_\sigma B \frac{\partial I_1}{\partial x;\, y} \tag{1}$$

where C_σ is the elasto-optic constant of the material, B is its initial thickness and $I_1 = (\sigma_x + \sigma_y)$ is the first stress invariant *for plane stress* condition and σ_x and σ_y denote the thickness-wise averages.

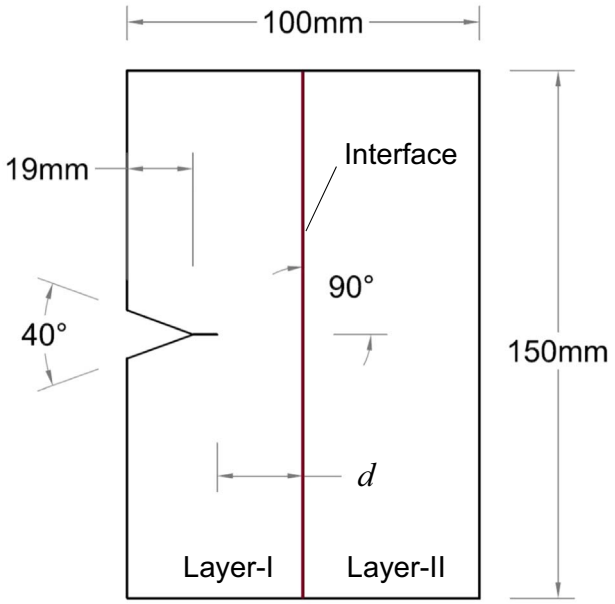

Fig. 3. Specimen configurations studied. Values of d used are 7 mm, 17 mm, 28 mm and 42 mm.

Table 1
Characteristics of Weldon 16 acrylic adhesive.

Adhesive characteristics	
Parameter	**Value**
Color	clear
Viscosity	800 cps
Working time	2–3 min
Fixure time	5–6 min
80% Strength	16 h
Specific gravity	1.02 ± 0.04

3. Specimen preparation and geometry

Two cast PMMA plates 170 mm tall, 8.6 mm thick and of different widths were joined along 170 mm × 8.6 mm faces using an acrylic adhesive to form bilayer specimens. The bonding surfaces were sanded using 400grit sandpaper and then cleaned to remove any residue before joining. The cured specimens were machined to their final dimensions of 150 mm × 100 mm × 8.6 mm (see Fig. 3). The adhesive used was Weldon 16, a transparent acrylic adhesive, to produce plates that were elastically homogeneous but had a discrete plane of weakness. An interface thickness of 100 μm was maintained in all specimens using shims (spacers) while bonding the plates. The crack initiation toughness for the joint was ~50% of the virgin PMMA (Sundaram and Tippur, 2016). Other details of this adhesive are listed in Table 1. A 40° V-notch was machined at the mid-span of the first layer. The notch was extended into the plate by 2 mm using a 300 μm thick diamond impregnated circular saw resulting in a total notch length 'a' of 21 mm. The extended notch tip was subsequently sharpened by scoring it with a razor blade. The bilayer specimens had an interface at four different distances (designated by 'd' in Fig. 3), 7 mm, 17 mm, 28 mm and 42 mm from the sharpened tip. These correspond to d/a ratios of 0.33, 0.81, 1.33, and 2.0, respectively. The dynamic properties of PMMA are listed in Table 2.

4. Experimental setup and procedure

The dynamic fracture of PMMA bilayers were studied using transmission-mode DGS in conjunction with ultrahigh-speed digital photography. The schematic of the experimental setup employed is shown in Fig. 4. A Hopkinson pressure bar was used for loading the pre-notched specimen. It was a 1.83 m long-bar of 25.4 mm diameter with a wedge shaped tip pressed against an unconstrained bilayer specimen with the matching V-notch (see, Fig. 5). A 305 mm long, 25.4 mm diameter rod

Table 2
Some properties of cast PMMA.

Dynamic Properties of PMMA	
Parameter	Dynamic Value
Density	1010 kg/m^3
Elastic modulus	5.0 GPa
Poison's ratio	0.34
Elasto-optic constant	-1.08×10^{-10} m^2/N

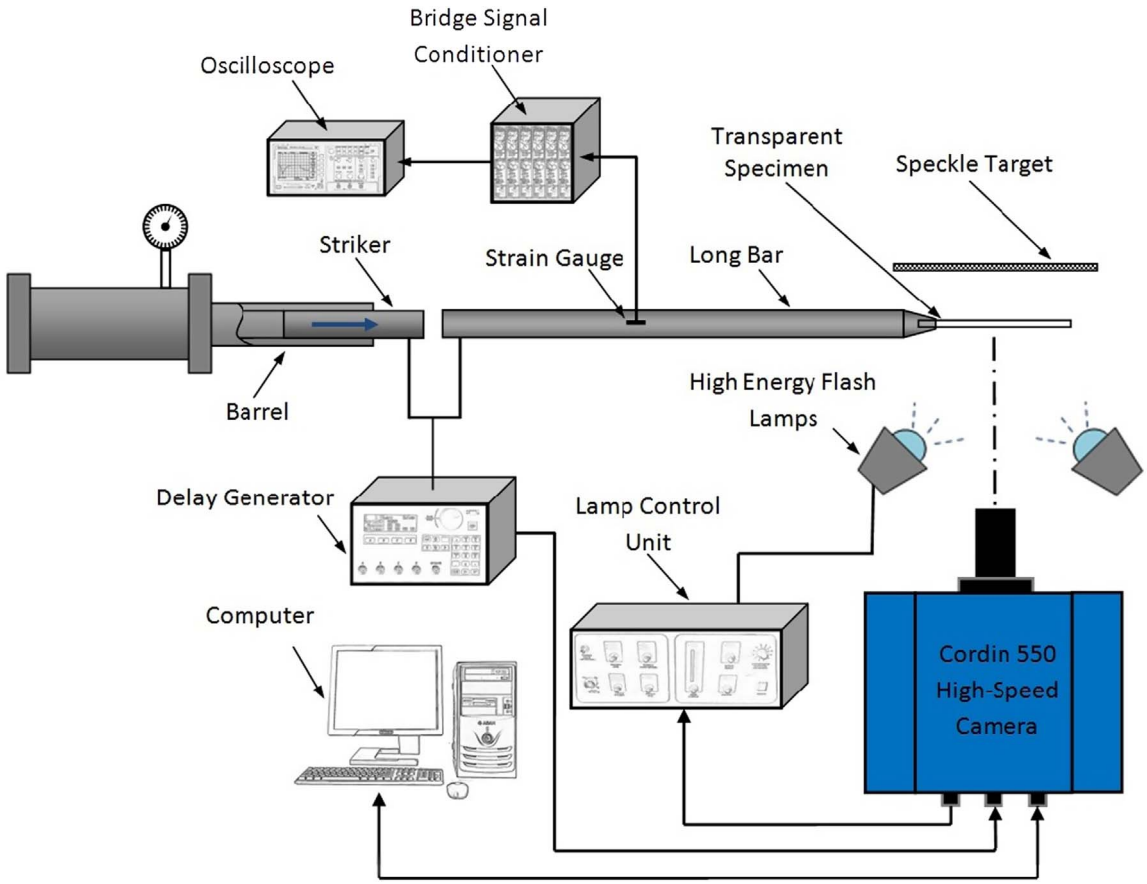

Fig. 4. Schematic of the experimental setup (top view) used for dynamic fracture study.

held inside the barrel of a gas-gun was co-axially aligned with the long-bar and was used as the striker. Both the long-bar and the striker were made of AL 7075-T6 eliminating the impedance mismatch between them during impact.

The speckle images were acquired using a Cordin-550 ultrahigh-speed digital camera with a sensor resolution of 1000×1000 pixels and 32 independent CCD sensors positioned radially around a five-facet rotating mirror. The imaging system also included two high-energy flash lamps producing broad-band white light illumination. Experimental parameters such as the trigger delay, flash duration, framing rate, CCD gain, and data storage were controlled using a computer connected to the camera. A 28–300 mm focal length macro zoom lens mounted on an adjustable bellows was used for imaging the dynamic event. Further, the lens aperture was kept open as widely as possible (numerical aperture F$^{\#}$5.6) to achieve a good exposure with minimum electronic gain setting during photography. The specimen was at a distance of approximately 850 mm in front of the camera. (Each speckle covered approximately 4–5 pixels; or, the scale factors of 22–24 pixels/mm were used.) The specimen was placed on an adjustable platform with a 2 mm thick strip of putty pressed on the top and bottom edges of the specimen, as shown in Fig. 5. The putty strips helped to achieve symmetric, approximately free surface boundary conditions at the top and bottom edges. A target plate decorated with random black and white speckles was placed behind the specimen at a distance $\Delta=29.3$ mm from the mid-plane of the specimen. A pair of heavy dots (Fig. 6) was

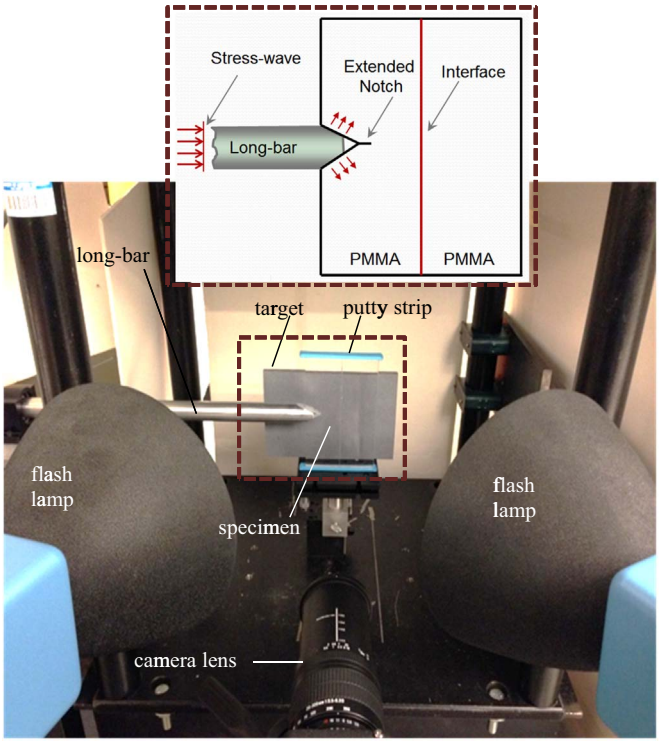

Fig. 5. Close-up photograph of the experimental setup used in dynamic fracture experiments (Inset: schematic of the loading configuration used).

marked on the target plate to help relate the dimension on the image to the actual specimen/target dimensions during image analysis.

The region of interest in this study was in the neighborhood of the interface. Accordingly, the camera was focused on a 45 mm × 45 mm square region on either side of the (vertical) interface. Prior to loading, a set of 32 images of the speckles were recorded in the undeformed state at 200,000 frames per second. (The choice of the framing rate was to balance information gathered over the entire event covering crack growth in layer-I, along the interface, and in layer-II with good spatial as well as temporal detail, and within the capabilities of the camera.) Sufficient care was exercised to achieve an approximately Gaussian distribution of gray scales for each image, typically in the mid-range of 0–255 (8 bit) gray scale by adjusting the flash lamps. Next, without altering any of the camera settings, the striker was launched towards the long-bar at a velocity of ~15 m/s. When the striker contacted the long-bar, a compressive stress-wave was set-off in the long-bar, which propagated over its length before loading the specimen along the two inclined faces of the V-notch. The duration of the stress pulse generated was ~120 μs. When the striker contacted the long-bar, a trigger signal was also produced. This initiated the camera to record a second set of 32 images in the deformed state at the same framing rate. A trigger delay, different for each interface location, was used to adjust the time window due to the fixed number of frames (32) that could be recorded by the camera. Thus, a total of 32 pairs of images in the deformed and undeformed (reference) states were recorded at 5 μs intervals between successive images. Two representative speckle images in the region of interest, one in the undeformed state and the other in deformed state for a layered specimen configuration, are shown in Fig. 6. It can be seen that the speckles are noticeably distorted in the vicinity of the propagating crack-tip (in the deformed image) whereas they are largely unaffected in the far-field. The interface is evident as a translucent vertical line at the center of each image. The corresponding two images for each sensor were paired from the undeformed and deformed sets and each of these 32 matched pairs was correlated separately.

5. Image analysis and evaluation of crack-tip parameters

The 2D digital image correlation was carried out using the image analysis software ARAMIS®. During analysis, each image was segmented into facets/sub-images consisting of 25 × 25 pixels. An overlap of 20 pixels (i.e., step size of 5 pixels) was used during image correlation. This resulted in 194 × 194 matrix of data points in the region of interest for each of the two orthogonal displacement fields. The corresponding angular deflections of light rays were subsequently determined using the known distance Δ between the specimen and the target planes.

The position of the crack-tip in each digitized image was used to measure the instantaneous crack length. This typically includes errors in the crack extension data and hence the computed crack velocity histories. To minimize the errors, a quadratic Bézier curve (Prautzsch et al., 2002; Jajam and Tippur, 2012) was fitted to the crack length data at a time instant '*i*' as,

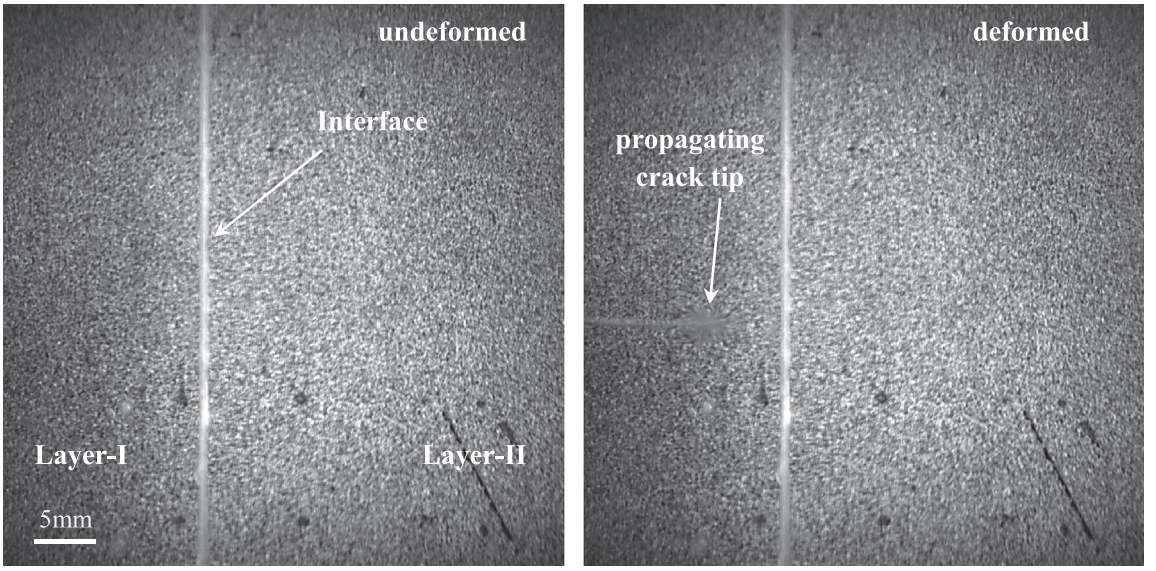

Fig. 6. Speckle images in the undeformed (left) and deformed (right) states recorded by the high-speed camera through a PMMA bilayer.

$$a_i(s) = (1-s)^2\hat{a}_i + 2s(1-s)\hat{a}_{i+1} + s^2\hat{a}_{i+2}, \quad 0 \le s \le 1 \tag{2}$$

where s, $\hat{a}$ and a are the smoothing parameter, the digitized crack length, and the smoothed crack length, respectively. In the above expression $\hat{a}_i$, $\hat{a}_{i+1}$, $\hat{a}_{i+2}$ are the control points of $a_i(s)$. The value of s was 0.5 such that the smoothed data point is at the middle of the interval. Subsequently, the crack velocity (V) was estimated from the smoothed crack length history using backward difference method,

$$V_i = \frac{a_i - a_{i-1}}{t_i - t_{i-1}} \tag{3}$$

where a and t are crack length and time, respectively.

Using the two orthogonal angular deflection fields, the instantaneous crack-tip fields in the local coordinates $(x',\ y')$(x' coincides with the local crack growth direction) for a moving crack were obtained by performing coordinate transformation. The mode-I and mode-II SIFs were evaluated from an over-deterministic least-squares analysis of the crack-tip data in conjunction with the asymptotic equation (See (Sundaram and Tippur, 2016) for details),

$$\begin{aligned}\phi_{x'}(t) &= \phi_x(t)\cos\ \theta(t) + \phi_y(t)\sin\ \theta(t)\\ &= C_\sigma B\left[\begin{array}{l} -\frac{1}{2}r_l^{-\frac{3}{2}}\left\{\begin{array}{l} f(V;\,C_L;\,C_S)A_1(t)cos\left(\frac{3\theta_l}{2}\right)\\ +g(V;\,C_L;\,C_S)D_1(t)\sin\left(-\frac{3\theta_l}{2}\right)\end{array}\right\}\\ +\sum_{N=2}^{\infty}\left\{\begin{array}{l} A_N(t)\left(\frac{N}{2}-1\right)r_l^{\left(\frac{N}{2}-2\right)}cos\left(\left(\frac{N}{2}-2\right)\theta_l\right)\\ +D_N(t)\left(\frac{N}{2}-1\right)r_l^{\left(\frac{N}{2}-2\right)}\sin\left(\left(\frac{N}{2}-2\right)\theta_l\right)\end{array}\right\}\end{array}\right]\end{aligned} \tag{4}$$

where f and g are functions of instantaneous crack velocity, and $(r_l,\ \theta_l)$ denote the contracted crack-tip polar coordinates, C_σ is the elasto-optical constant of the material, and B is its initial thickness. Further, $(r_l,\ \theta_l)$ can be expressed in the local Cartesian coordinates (x', y') as, $r_l = \left\{(x')^2 + \alpha_L{}^2(y')^2\right\}^{1/2}$ and $\theta_l = \tan^{-1}\left(\frac{\alpha_L y'}{x'}\right)$. The coefficients $A_1(t)$ and $D_1(t)$ in the asymptotic series are related to the mode-I and mode-II stress intensity factors $K_I(t)$ and $K_{II}(t)$, respectively, as $A_1(t) = K_I(t)\sqrt{\frac{2}{\pi}}$ and $D_1(t) = K_{II}(t)\sqrt{\frac{2}{\pi}}$. The functions f and g are,

$$f(V;\,C_L,\,C_S) = \left(\frac{1+\nu}{1-\nu}\right)\frac{(1+\alpha_S{}^2)(1-\alpha_L{}^2)}{4\alpha_L\alpha_S - (1+\alpha_S{}^2)^2} \text{ and } g(V;\,C_L,\,C_S) = \left(\frac{1+\nu}{1-\nu}\right)\frac{2\alpha_S(1-\alpha_L{}^2)}{4\alpha_L\alpha_S - (1+\alpha_S{}^2)^2} \tag{5}$$

where $\alpha_L = \left[1 - \frac{\rho(1-\nu)}{2\mu}V^2\right]^{\frac{1}{2}}$ and $\alpha_S = \left[1 - \frac{\rho}{\mu}V^2\right]^{\frac{1}{2}}$ for plane stress, μ and ρ are shear modulus and mass density, respectively. Data in the region $(0.25 < r/B < 0.75)$ and $(-135^\circ < \theta < 135^\circ)$ near the crack-tip was used for analysis. Since mixed-mode crack growth occurred in some cases, the SIFs were used to evaluate the *effective* SIF (K_{eff}) and mode-mixity (ψ) using,

$$K_{eff}(t) = \sqrt{K_I^2(t) + K_{II}^2(t)}, \quad \tan\ \psi(t) = \frac{K_{II}(t)}{K_I(t)}. \tag{6}$$

6. Experimental results

6.1. Crack paths and deformation histories

Photographs of four fractured samples, one from each configuration (interface at $d=7$ mm, 17 mm, 28 mm, and 42 mm from the initial tip), are shown in Fig. 7. The stress-wave loading occurred near the left edge of the specimen on the faces of the V-notch and the crack propagation direction was from left to right, as shown by the arrowhead. In each case it is evident that the crack propagated self-similarly until it reached the interface vicinity. The crack paths differed subsequently. For all configurations except the one where the interface was the nearest to the initial tip, the mode-I crack in the first layer arrived at the interface, lodged into the interface, bifurcated into two interface crack-tips, one propagating upwards and the other downwards, and then both penetrated the second layer simultaneously after some amount of interfacial crack growth. The extent of interfacial crack growth and the angle of emergence of the crack into the second layer varied with the position of the interface from the initial crack-tip. Fig. 7(a) shows the crack path for the $d=7$ mm configuration and Fig. 7(b)–(d) for $d=17$ mm, 28 mm, and 42 mm configurations, respectively. For an interface location of $d=7$ mm, the mode-I crack propagated towards the interface and then grew past the interface into the second layer in a self-similar fashion without any visible branching until it reached the final third of the specimen. Beyond that, it modestly deviated from its initial path due to a loss of in-plane constraint (Maleski et al., 2004) as it approached the free edge. In Fig. 7(b)–(d), more nuanced fracture patterns involving mixed-mode interfacial crack growth and crack penetration into layer-II are evident. That is, the location of the interface dictated the crack path selection and the fracture behavior. This clearly shows that the introduction of the interface does not always produce crack branching but the location of the interface within the given geometry and the associated differences in crack-tip parameters determine the creation of new surfaces. Further, in $d=17$ mm, 28 mm, and 42 mm configurations, the trapped interface cracks traveled over distances of approximately 2 mm, 12 mm, 16 mm, respectively, along the interface, a monotonic increase, before emerging into the second layer as two daughter cracks at angles $\pm 28^\circ$, $\pm 18^\circ$, $\pm 11^\circ$ with respect to the initial tip direction, a monotonic decrease. These experiments were quite repeatable as shown in Appendix-A.

Plots of measured angular deflection contours ϕ_x and ϕ_y proportional to orthogonal stress gradients $(\sigma_x + \sigma_y)_{,x}$ and $(\sigma_x + \sigma_y)_{,y}$ (the comma notation denotes derivatives with respect to the subscript) obtained from the image correlation for two select configurations namely, $d=7$ mm and 42 mm are shown in Figs. 8 and 9, respectively. Further, note that the plots presented are only for three select time instants for the sake of brevity. (The angular deflection contours, the contour levels and the scale bar are shown in the first plot in each set and are applicable to the other plots as well.) In these $t=0$ μs represents the time at which the crack initiated at the original notch tip.[3] In each figure, sets (a) and (b) correspond to contours of ϕ_x and ϕ_y, respectively.

Fig. 8 shows angular deflection contours for $d=7$ mm configuration. The crack followed a nearly straight path during the time window of interest, both in layer-I and -II without detectable propagation along the interface. This behavior is similar to the monolithic specimen studied by the authors previously (Sundaram and Tippur, 2016) and suggests that there was little effect of the interface on the crack trajectory. The overall size of the contours changed during crack growth implying a variation of stress intensity factors during the window of observation. (It should also be noted that ϕ_x contours are symmetric in shape and magnitude with respect to the growing crack path whereas ϕ_y contours are only symmetric in shape but anti-symmetric in magnitude.) Fig. 9 shows angular deflection contours for $d=42$ mm configuration. Initially the crack traveled self-similarly in layer-I as in $d=7$ mm configuration. When it neared the interface, however, perturbations in the outer contours ahead of the crack-tip for ϕ_x are evident. At a later instant, it can be seen that the crack is propagating along the interface as two globally symmetric (with respect to the initial crack growth or the x-direction) daughter cracks which are about to kink into layer-II. Subsequently, the two daughter cracks emerge from the interface into layer-II and propagate nearly symmetrically, but in mixed-mode condition as evident from asymmetric (relative to crack growth direction), tri-lobed contours typical of crack-tip stress gradient fields (Tippur and Rosakis, 1991).

Similar features at various time instants were observed in the angular deflection contours for $d=17$ mm and 28 mm configurations as well but are not shown for the sake of brevity. Major differences were the extent of crack growth along the interface and angle of emergence of the two daughter cracks into layer-II.

[3] Separate experiments were carried out in which the region of interest was around the initial crack-tip to determine the time at which crack initiated and this data was used to compile the fracture histories of various configurations into a single timeline. Details are suppressed for brevity.

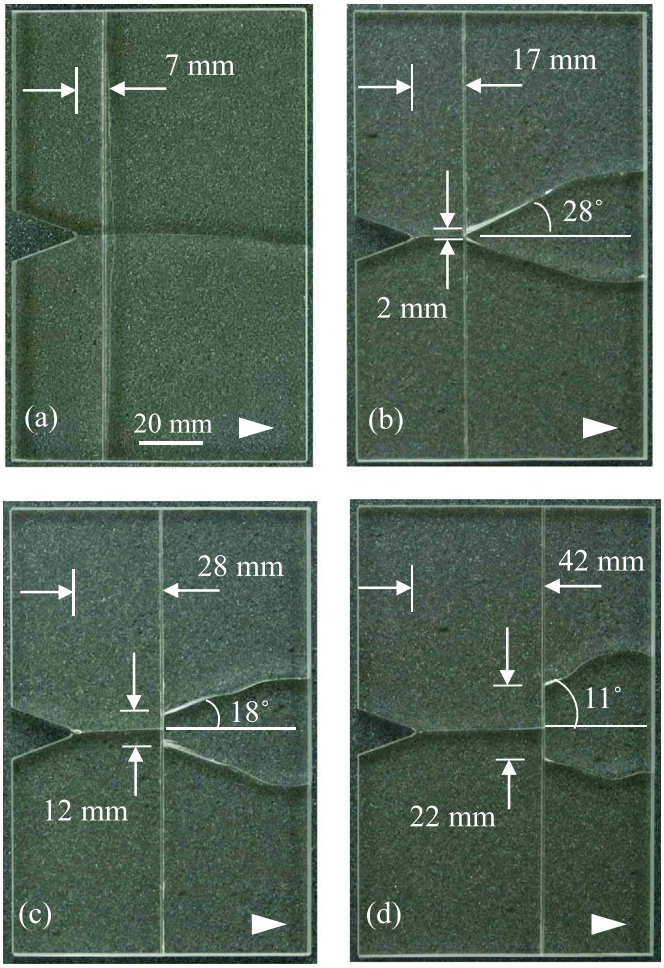

Fig. 7. Photographs of fractured specimens showing crack path selection in d = (a) 7 mm, (b) 17 mm, (c) 28 mm, and (d) 42 mm configurations, respectively. Arrowheads indicate crack growth direction.

6.2. Crack velocity histories

Fig. 10 shows plots of crack velocity histories for all the four configurations. (Note that these histories correspond to the upper branch of the branched crack configurations; the lower branches show similar history in each case (Sundaram and Tippur, 2016)). It should be noted that $t=0$ μs represents the time at which the crack initiated at the original notch tip. The solid-line circle marked on each of these plots represents the value at an instant before the crack enters the interface and the dotted-line circle represents the instant at which the crack emerges from the interface. (For $d=7$ mm, 17 mm, 28 mm, and 42 mm cases,[4] the crack velocities upon the arrival at the interface were approximately 265 m/s, 326 m/s, 370 m/s, 441 m/s, respectively.) From the figure it can be seen that the velocity histories for $d=17$ mm, 28 mm and 42 mm configurations all follow a similar pattern whereas $d=7$ mm configuration has a distinctively different behavior. In the former cases, the crack velocity transitioned from a lower to a higher value as the tip approached the interface. When it entered the interface and transitioned from being a single mode-I crack to bifurcated interfacial cracks, the velocity increased rapidly to a (different) peak value in each case. These peak velocities attained during interfacial propagation increased monotonically with the interface distance d from the initial crack-tip. The peak velocities were approximately 440 m/s, 528 m/s and 824 m/s for $d=17$ mm, 28 mm and 42 mm configurations, respectively. Following the rapid increase in velocity, an equally steep drop, generally close to or below the value corresponding to the one at the entrance to the interface occurred. Subsequently, these crack-tips broke out of the interface simultaneously and into layer-II as mixed-mode cracks at speeds lower than the corresponding initial velocities. Further, it can be seen from Fig. 10 that the crack velocity for $d=42$ mm configuration towards the end of the event (after $t\sim220$ μs) was as low as ~170 m/s. In contrast to these cases, in $d=7$ mm configuration it can be

[4] The crack velocity upon arrival at the interface for an interface distance of $d=28$ mm and a higher interface toughness ($K_{Ic}=1.02$ MPa$\sqrt{\text{m}}$) reported in the previous study (Sundaram and Tippur, 2016) was ~365 m/s.

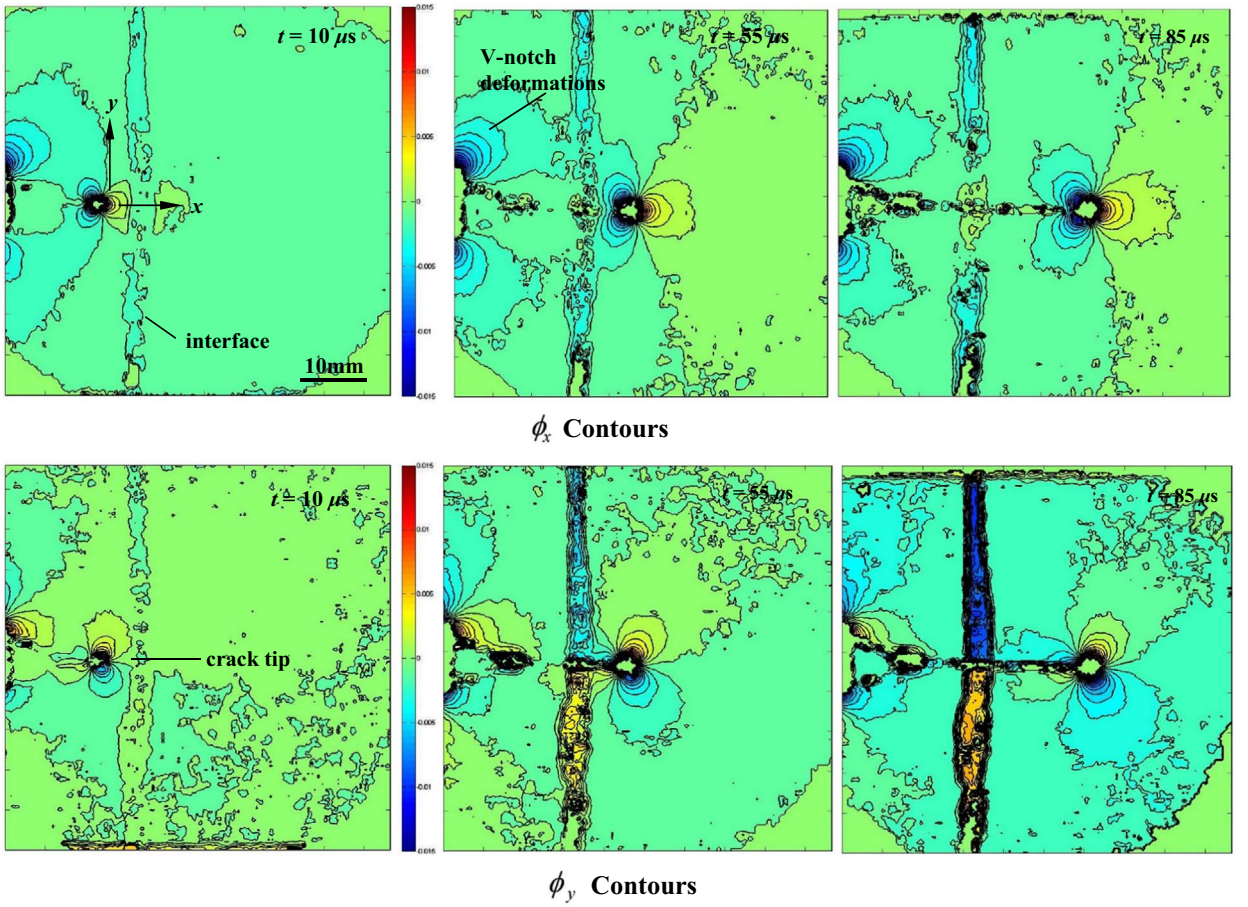

Fig. 8. Angular deflection contour plots (contour interval$=1\times10^{-3}$ rad) proportional to stress gradients of $(\sigma_x+\sigma_y)$ in the x- and y-directions for a $d=7$ mm configuration. (Time $t=0$ corresponds to crack initiation at the original notch tip.).

observed that the velocity increased when the crack approached the interface but it continued to gain speed rather smoothly as it propagated past the interface without interfacial growth, eventually attaining a maximum velocity of ~394 m/s before slowing down as it propagated further into layer-II to a final velocity of ~283 m/s during the observation window.

6.3. SIF histories

The effective SIF histories (K_{eff}) and the corresponding mode-mixity (ψ) variations evaluated from DGS for all configurations are plotted in Fig. 11(a) and (b), respectively. (The details on determining the mixed-mode SIFs have been previously reported by the authors (Sundaram and Tippur, 2016) Similar to the velocity histories, the effective SIF histories of the three branched configurations, namely, $d=17$ mm, 28 mm and 42 mm, showed similarities whereas it was distinctively different in case of the unbranched ($d=7$ mm) configuration. (Again, these histories correspond to the upper branch of the bifurcated cracks.) In each of these cases, K_{eff} values increased as the mode-I crack approached the interface, reaching a maximum when it was about to enter the interface. As the interfacial debonding and bifurcated crack growth ensued along the interface, a steep drop in K_{eff} occurred in each of these cases. Following a gradual recovery from this low value after the steep drop, the interface crack kinked into layer-II at a K_{eff} lower than the one at the entrance to the interface. As the mixed-mode crack growth in layer-II continued, a steady drop in the K_{eff} values, sometimes below the nominal crack initiation toughness values of the virgin material, were seen. On the contrary, in the unbranched case ($d=7$ mm), K_{eff} increased monotonically as the crack reached the interface, penetrated the interface and then layer-II. The peak value of K_{eff} occurred when the crack-tip had grown past the interface and into layer-II before dropping steadily at later stages.

In all of the three branched crack configurations,[5] it can be seen that the peak value of K_{eff} occurred right before the crack entered the interface and there is a successive reduction in the peak value as the interface is moved farther from the initial crack-tip, i.e., 1.88 MPa$\sqrt{\text{m}}$, 1.57 MPa$\sqrt{\text{m}}$ and 1.41 MPa$\sqrt{\text{m}}$, respectively (solid-line circles). It can also be seen that there is a

[5] The measured effective SIF for the crack upon its arrival at the interface for an interface distance of $d=28$ mm and a higher interface toughness ($K_{Icr}=1.02$ MPa$\sqrt{\text{m}}$) reported in the previous study (Sundaram and Tippur, 2016) was ~1.48 MPa$\sqrt{\text{m}}$.

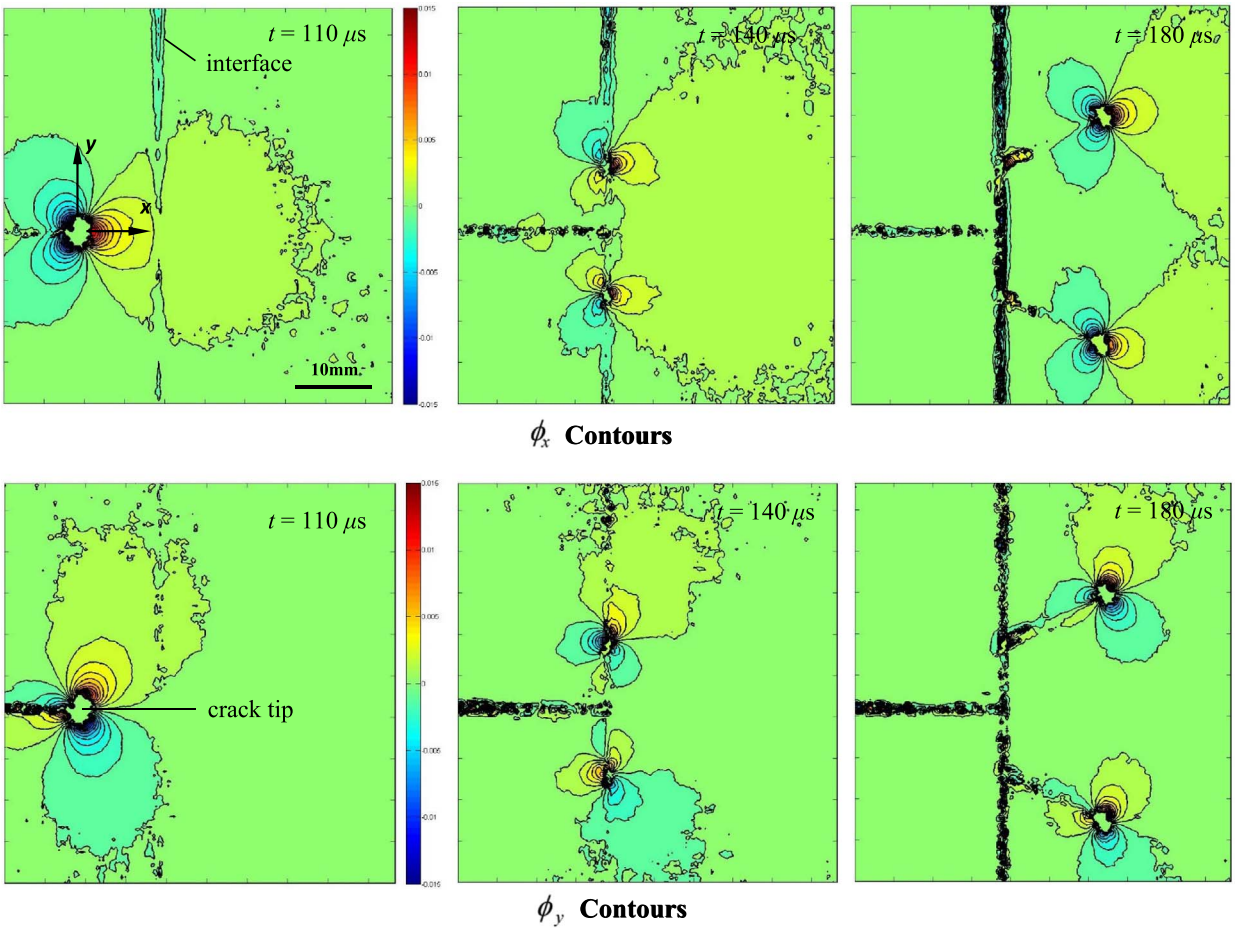

Fig. 9. Angular deflection contour plots (contour interval $=1\times10^{-3}$ rad) proportional to stress gradients of $(\sigma_x+\sigma_y)$ in the x- and y-directions for a $d=42$ mm configuration. (Time $t=0$ corresponds to crack initiation at the original notch tip.)

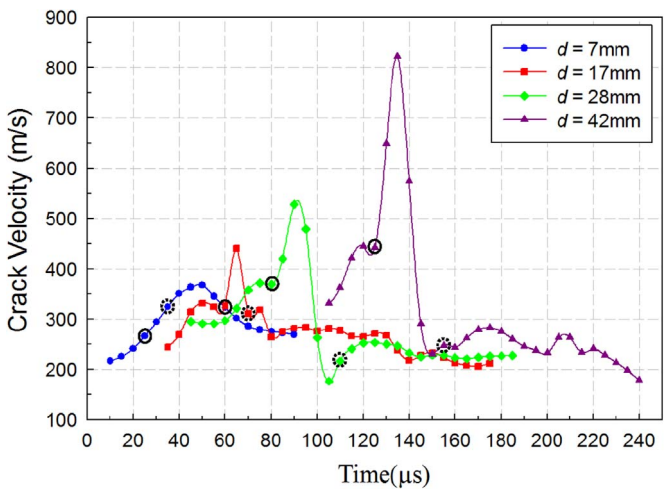

Fig. 10. Crack velocity histories for all the four configurations investigated. The solid-line circles represent the instant before the crack enters the interface and the dotted-line circles represent the instant at which crack emerges from the interface. (Time $t=0$ corresponds to crack initiation at the original notch tip.).

decrease in the final value of K_{eff} in layer-II as the interface is positioned farther from the initial crack-tip, i.e., 0.95 MPa$\sqrt{\text{m}}$, 0.81 MPa$\sqrt{\text{m}}$ and 0.73 MPa$\sqrt{\text{m}}$, respectively. In the unbranched specimen configuration, the effective SIF increased gradually from 1.07 MPa$\sqrt{\text{m}}$ (at $\sim$10 μs after initiation) as it propagated in layer-I. When the crack propagated past the

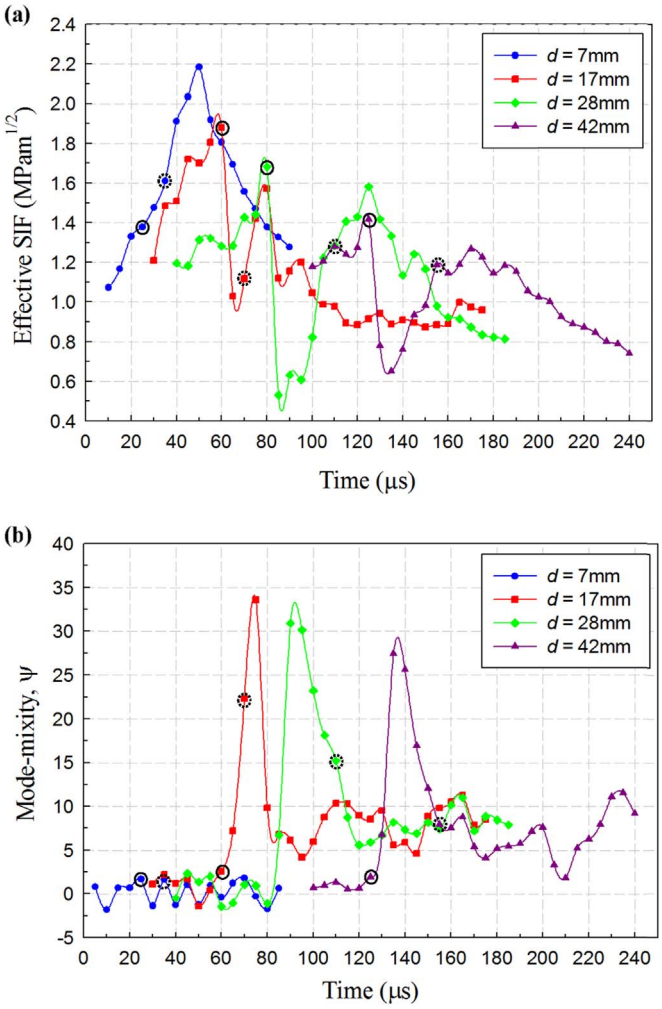

Fig. 11. Time history of crack tip parameters (Time t=0 corresponds to crack initiation at the original notch tip) for all the four configurations investigated: (a) Effective stress intensity factor histories and (b) mode-mixity histories. The solid-line circles represent the instant before the crack enters the interface and the dotted-line circles represent the instant at which crack emerges from the interface; note that there is greater uncertainty with crack kinking out of the interface.

interface into layer-II the effective SIF continued to gradually increase reaching a peak value of 2.38 MPa$\sqrt{\text{m}}$ and then dropped back to 1.35 MPa$\sqrt{\text{m}}$ at the end of the observation window.

The mode-mixity ψ (Fig. 11(b)) for the three branched cases show similar variation whereas the one for the unbranched configuration is nearly zero in the observation window. In the former three cases, as the crack transitioned from layer-I into the interface, a steep increase in ψ occurred due to increased mode-II SIF. The mode-mixity values when the cracks kinked into layer-II vary, the highest being for $d=17$ mm configuration and the lowest for $d=42$ mm case. This pattern is consistent with the measured angles of crack emergence noted in Fig. 7.

7. Discussion

7.1. Crack penetration vs. branching mechanism

The observed crack penetration or branching at an interface was examined using measured fracture parameters, namely, the instantaneous crack velocity V and SIF K_I for each of the configurations. This was done by evaluating stresses at a point directly ahead of the propagating crack-tip but situated on the interface. The position of the crack-tip in each image was used to measure the instantaneous distance of the point interest on the interface (r_i). Knowing $\theta = \theta_i = 0$ at the point of interest, the stresses were evaluated using K-dominant expressions (Freund, 1998),

$$\sigma_{ij} = \frac{K_I(t)}{\sqrt{2\pi r}}\,\Sigma_{ij}(\theta = 0,\ V), \quad i,j = x,y \tag{7}$$

where

$$\Sigma_{xx} = \frac{1}{D}\left\{\frac{\left(1+\alpha_S^2\right)\left(1+2\alpha_L^2-\alpha_S^2\right)}{\sqrt{\gamma_L}}\cos\left(\frac{\theta_L}{2}\right) - \frac{4\alpha_S\alpha_L}{\sqrt{\gamma_S}}\cos\left(\frac{\theta_S}{2}\right)\right\}$$

$$\Sigma_{yy} = -\frac{1}{D}\left\{\frac{(1+\alpha_S^2)^2}{\sqrt{\gamma_L}}\cos\left(\frac{\theta_L}{2}\right) - \frac{4\alpha_S\alpha_L}{\sqrt{\gamma_S}}\cos\left(\frac{\theta_S}{2}\right)\right\},$$

$$\Sigma_{xy} = \frac{2\alpha_L\left(1+\alpha_S^2\right)}{D}\left\{\frac{1}{\sqrt{\gamma_L}}\sin\left(\frac{\theta_L}{2}\right) - \frac{1}{\sqrt{\gamma_S}}\sin\left(\frac{\theta_S}{2}\right)\right\},$$

$$D = 4\alpha_S\alpha_L - \left(1+\alpha_S^2\right)^2, \quad \alpha_{S;L} = \sqrt{1-\left(\frac{V}{C_{S;L}}\right)^2},$$

$$\gamma_{S;L} = \sqrt{1-\left(\frac{V\ \sin\ \theta}{C_{S;L}}\right)^2}, \quad \tan\ \theta_{S;L} = \alpha_{S;L}\ \tan\ \theta.$$

In the above, $K_I(t)$ is the instantaneous mode-I SIF, C_S and C_L are the shear and longitudinal wave speeds, and V is the crack velocity. Fig. 12(a)–(d) shows plots of instantaneous normal stress biaxiality $\left(\frac{\sigma_x}{\sigma_y}\right)_i$, $\left(\tau_{\max}^{2D}\right)_i\left(=\left|\frac{\sigma_x-\sigma_y}{2}\right|_i\right)$, $\left(\tau_{\max}^{3D}\right)_i\left(=\left|\frac{\sigma_x}{2}\right|_i\right)$ and $(\sigma_x)_i$ histories at the interface, directly ahead of the moving crack-tip until the crack arrives at the interface. (Note that double subscripts $xx=x$, $yy=y$ are dropped henceforth for simplicity.) All these stresses increase rapidly at the point of interest as the growing crack-tip approaches it (see Figs. 12, 13(a)). From these plots one could hypothesize a failure mechanism that involves nucleation of a (micro scale) debond at the point of interest on the interface due to one of these stresses exceeding the strength of the interface (see Fig. 13(b)). Based on the magnitude of $\left(\tau_{\max}^{2D}\right)_i$ relative to $\left(\tau_{\max}^{3D}\right)_i$ (Fig. 12 (a) and (b)) one could safely assume that $\left(\tau_{\max}^{3D}\right)_i$ or $(\sigma_x)_i$ likely to cause debond nucleation. By extrapolating these plots, $\left(\tau_{\max}^{3D}\right)_i$ and $(\sigma_x)_i$ values as the crack-tip arrives at the interface were estimated; they were approximately (9, 17, 22 and 30 MPa) and (18, 34, 44 and 60 MPa), respectively, for $d=7$ mm, 17 mm, 28 mm, and 42 mm configurations. The strength of the interface was also measured independently using asymmetric four-point-bend (Xu and Tippur, 1995) and direct tension experiments for the interface, as detailed in Appendix-B. The measured shear and tensile strengths of the interface were found to be 26 ± 0.5 MPa and 23 ± 0.3 MPa, respectively. The comparison between the strength and the induced interfacial stress as the crack-tip approached the interface suggests a tension $(\sigma_x)_i$ induced debond nucleation at the interface in the $d=17$ mm, 28 mm, and 42 mm cases and not a shear induced debond nucleation because the shear stress $\left(\tau_{\max}^{3D}\right)_i$ experienced by the interface is consistently lower than its shear strength (see Fig. 12(c) and (d)). As the crack approaches the interface, the *debond*–visualized as a crack with two equidistant singularities from the point of incidence–led to the unzipping of the interface in two opposite (upward and downward) directions over some length until it becomes energetically favorable for the crack to kink into and penetrate layer-II. In the $d=7$ mm case, however, the stresses were below the interfacial tensile strength and hence a debond did not nucleate, thereby allowing a successful penetration of the interface and layer-II by the incident mode-I crack without branching (see Fig. 13(c)).

In the branched crack cases, the kinking of the interface crack into layer-II was examined using the critical value of SIFs $\left(K_{eff}\right)_i\left(=\left(\sqrt{K_I^2+K_{II}^2}\right)_i\right)$ for the 100 μm thick interface at different mode-mixities (see Appendix B) and mixed-mode dynamic crack initiation toughness data for PMMA obtained from a complementary study (Sundaram and Tippur, in preparation). The dynamic crack initiation toughness of PMMA at different mode-mixities were obtained experimentally (using DGS and high-speed photography) and the details are suppressed here for brevity. In these experiments, single-edge cracked, free-standing plates (50 mm × 100 mm × 8.6 mm) were subjected to symmetric and asymmetric single-point impact loading relative to the crack-line, as show in Fig. 14 (inset). The stress-wave loading was imposed on the edge opposite to the cracked edge of the plate. In the asymmetric (eccentric) loading configurations, the length of the crack was varied between 6 mm and 15 mm (or, a/w ratio of 0.12–0.3) to generate different mode-mixities at initiation while keeping the eccentricity constant (= 15 mm). Deeper the crack, the higher was the mode-mixity at crack initiation. The critical values of K_I and K_{II} are plotted in Fig. 14 as solid circles. The fitted curve/band of data represents the dynamic fracture envelop for PMMA based on these experiments. The error band denotes (a) variability of SIF during analysis of optical data, and (b) repeatability of individual experiments.

The measured K_I and K_{II} at the instant the crack kinks or penetrates layer-II for the four different interface locations are plotted as green solid diamonds overlaid on the fracture envelop for PMMA in Fig. 14. Also included in this plot is the data point (brown solid diamond) from Sundaram and Tippur (2016) for the branched crack case for a relatively stronger interface (25 μm thickness and interface fracture toughness of ~75% that of virgin PMMA) compared to the ones studied in this work. A reasonably good agreement between the fracture envelop for PMMA and the solid diamonds corresponding to crack branching is notable despite the differences in the experimental conditions. On the other hand, the data point corresponding to direct penetration of layer-II without branching

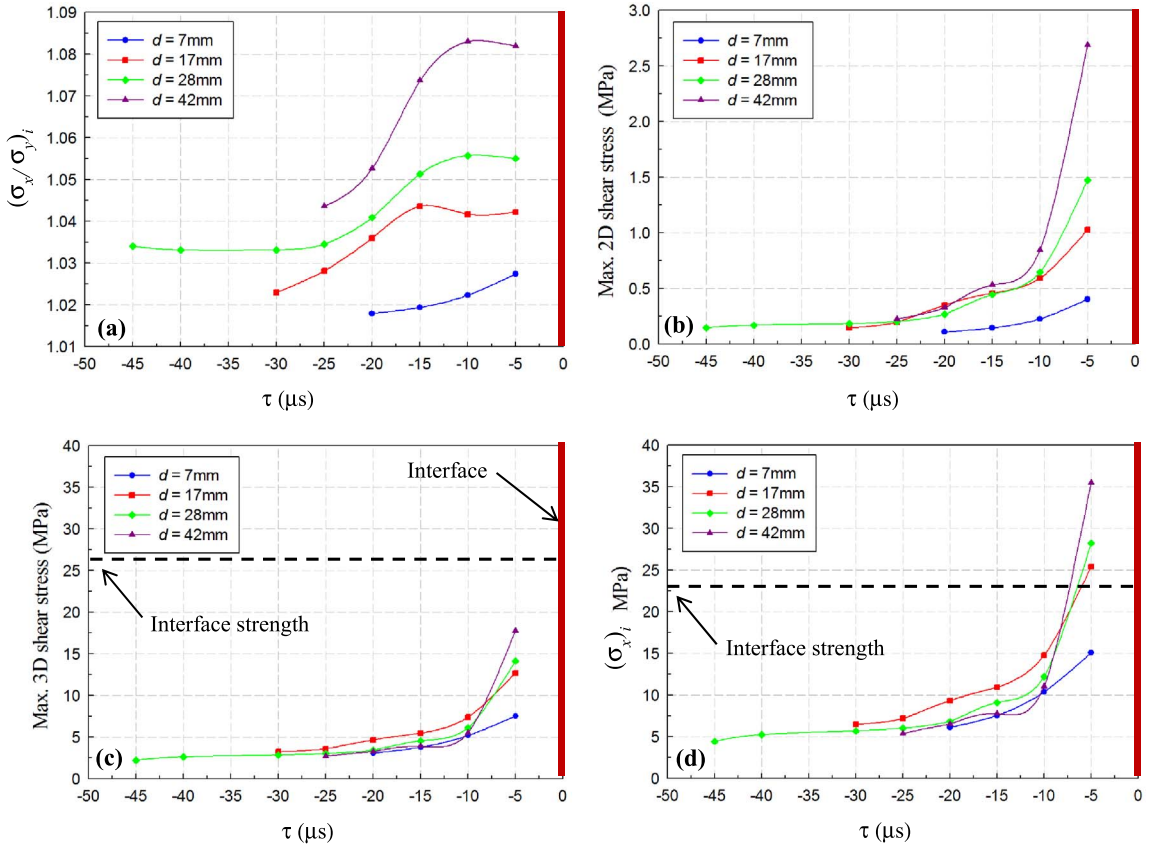

Fig. 12. Temporal evolution of stresses at a point on the interface directly ahead of the mode-I mother crack: (a) Ratio of in-plane normal stresses, (b) Maximum in-plane shear stresses, (c) Maximum shear stress, and (d) In-plane normal stresses in the crack growth direction. (τ=0 μs *corresponds to crack reaching the interface indicated by the heavy red line.*)

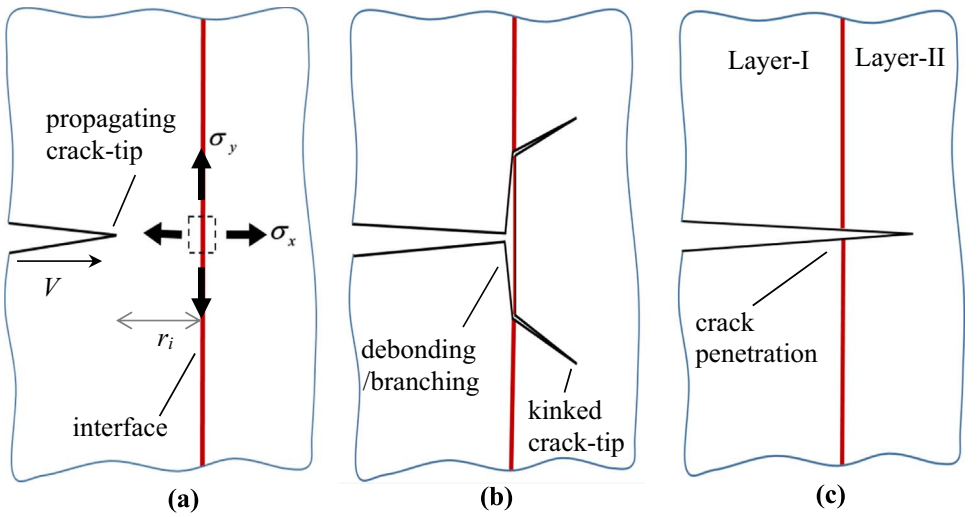

Fig. 13. Crack penetration vs. branching mechanism: (a) State of stress at a point on the interface ahead of an approaching mode-I crack in layer-I, (b) Nucleation of interfacial debond that facilitates crack branching, interfacial growth and crack kinking, (c) Unsuccessful nucleation of debond facilitates crack penetration into layer-II.

(red solid triangle) is clearly outside the fracture envelop, which is expected. Further, the tendency of the crack to kink out of the interface instead of continue propagating along the weak interface can be explained by the increasing critical *effective* SIF of the interface $\left(K_{eff}\right)_i$ with mode-mixity (see Appendix B) making it favorable for the daughter cracks to enter layer-II.

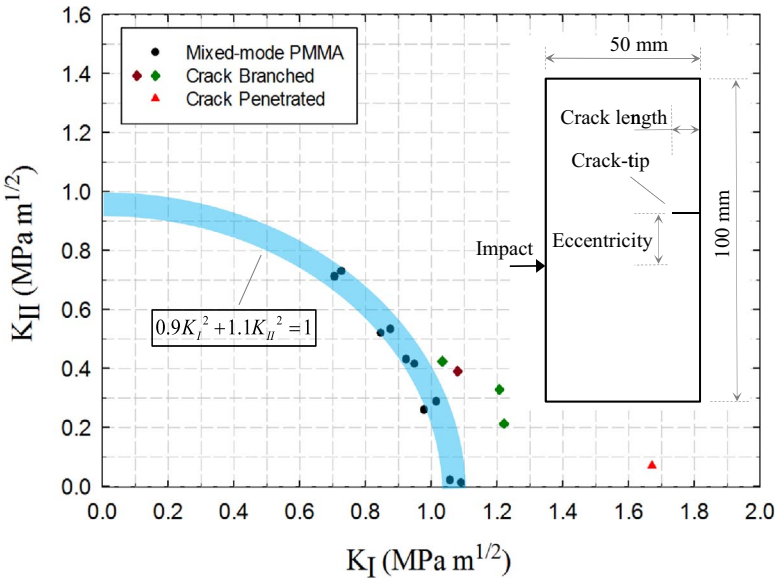

Fig. 14. Dynamic fracture envelope for PMMA. (For interpretation of the references to color in this figure, the reader is referred to the web version of this article.).

7.2. An empirical observation

As evident from Figs. 10 and 11, the crack velocity V and the effective SIF K_{eff} histories affect the penetration vs. branching phenomenon. That is, the crack velocities monotonically increased whereas the effective SIFs monotonically decreased when the crack-tip was about to enter the interface in the branched cases as the distance between the initial tip and the interface was increased. Based on the prevailing understanding of the mechanics of dynamic crack growth in brittle monolithic solids, the crack velocity is the parameter responsible for crack branching (Freund, 1998; Ravi-Chandar and Knauss, 1984). Other mode-I dynamic fracture investigations have suggested (Dally, 1979) K_I - V plots for a dynamically growing crack in a monolithic brittle solid as a material characteristic. However, suitable explanations for crack penetration vs. branching seen in this work do not exist. Further, the discussion in the previous section on tensile stress $(\sigma_x)_i$ induced disbond nucleation suggests that the stress intensity factor also plays a significant role in this branching/penetration mechanism. Taking these into consideration, possible existence of other quantifiable parameters involving crack velocity and effective SIF were examined. Among those considered the quantity $K_{eff} \times V$ showed a rather interesting behavior noted below:

A plot of $K_{eff} \times V$ histories for all configurations is shown in Fig. 15. The continuous circles represent the values of this parameter just before the crack entered the interface and the broken-line circles represent those just after the crack exited the interface. It can be seen that values of $K_{eff} \times V$ before the crack entered the interface (the continuous circles) in $d = 17$ mm, 28 mm, and 42 mm cases fall within a narrow band highlighted by the blue shaded strip at $\sim 600 \pm 25$ MPa m$^{3/2}$ s^{-1} whereas after exiting the interface (the broken circles) fall within yet another narrow band highlighted by the red shaded rectangle at 300 ± 25 MPa m$^{3/2}$ s^{-1}). From the previous study on a monolithic specimen of the same geometry and material by the authors , $K_{eff} \times V$ was evaluated as ~340 MPa m$^{3/2}$ s^{-1} during propagation. Further, recognizing that there are two branched cracks in layer-II in these cases, each having $K_{eff} \times V$ of ~300 MPa m$^{3/2}$ s^{-1}, is approximately one half of the corresponding value before the crack entered the interface from layer-I.[6] Although no mechanistic explanation for this observation is readily evident, it certainly is an interesting empirical observation that deserves scrutiny. Further, the values of $K_{eff} \times V$ for the case when the crack did not branch but simply penetrated the interface and layer-II as a mode-I crack do not follow these trends.

8. Conclusions

In this work, fracture events associated with a dynamically growing mode-I crack interacting with a normally oriented weak interface in an otherwise homogeneous sheet were studied experimentally to reveal the underlying crack penetration vs. branching mechanics. Acrylic bilayers with a distinct plane of weakness made by joining two PMMA plates along a straight interface using an

[6] The $K_{eff} \times V$ for the crack-tip upon arrival at the interface for an interface distance of $d = 28$ mm and a higher interface toughness ($K_{Icr} = 1.02$ MPavm) reported in the previous study [1] was ~580 MPa m$^{3/2}$ s^{-1} and ~285 MPa m$^{3/2}$ s^{-1} after penetrating the interface. These fall into the two data bands for branched cracks in Fig. 15.

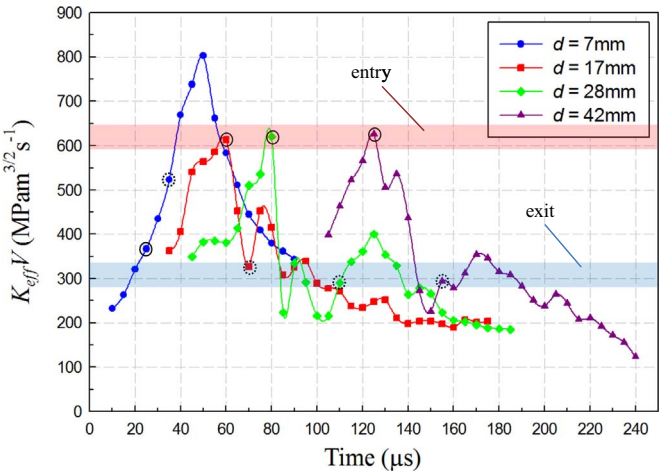

Fig. 15. $K_{eff} \times V$ histories for all four bilayer configurations. The closed circle represents the instant before the crack entered the interface and the broken circles represent the instant at which crack emerged from the interface. Crack tip data corresponding to before and after the interface fall into two distinct bands for branched cracks and the former is approx. twice that of the latter.

acrylic adhesive were examined. A gas-gun assisted long-bar impactor with a wedge shaped tip pressed into a matching V-notch cut along the edge of the specimen was used to dynamically initiate a mode-I crack in the first layer. Dynamic penetration and bifurcation of the mode-I crack upon its arrival at the interface were produced in a controlled manner by positioning the interface at four different distances from the initial crack-tip. The deformations in the crack-tip vicinity were evaluated optically using Digital Gradient Sensing (DGS) technique and ultrahigh-speed photography. The optical measurements were used in conjunction with the prevailing crack-tip field descriptions to extract stress intensity factors along with crack length and velocity histories during the dynamic event. Independent evaluation of interfacial tensile and shear strengths and fracture toughness was carried out to explain the witnessed phenomena and a rich array of mechanics. The major observations and conclusions of the work are as follows:

- The mode-I crack penetrated the interface and the second layer (layer-II) of the bilayer un-perturbed when the interface was located near the initial crack-tip. On the other hand, when the interface was located farther away from the interface, the mode-I mother crack bifurcated into two interfacial cracks, propagated in the opposite directions by nearly equal length and then penetrated the second layer as two mixed-mode daughter cracks all the while maintaining global symmetry relative to the loading/specimen geometry.
- In cases when the mode-I mother crack bifurcated at the interface, the amount of interfacial crack growth increased with the initial distance of the interface whereas the kink angle and hence the mode-mixity of the penetrated cracks as they entered the second layer decreased. Eventually, both the daughter cracks showed a tendency to attain mode-I condition.
- From the measured crack velocity histories it was observed that the crack simply penetrated the interface and the second layer as a mode-I crack when the crack velocity upon its arrival at the interface was the lowest among the four cases whereas it bifurcated and grew interfacially at higher incident velocities. This is counter to the intuition.
- The stress intensity factor histories examined in conjunction with the dynamic crack-tip fields suggest that at higher incident crack velocities, the interface directly ahead of the crack-tip experienced a large enough tensile stress, exceeding the strength of the interface, nucleating a micro debond before the arrival of the mode-I mother crack, resulting in two interfacial daughter cracks growing in opposite directions along the interface. The amount of interfacial crack growth increased with the incident crack velocity and continued until penetration into the second layer was energetically favorable due to competition between mixed-mode crack growth along the interface and mixed-mode crack growth into the subsequent layer.
- An interesting empirical observation involving the resultant (effective) stress intensity factor and crack velocity at the instant of crack incidence on the interface in each of the three branched crack configurations showed the product $K_{eff} \times V$ to be nearly a constant. Further, the corresponding values for each branched mixed-mode daughter crack when the second layer was penetrated were approximately one half of the corresponding incident value of $K_{eff} \times V$. The implications of this observation are, however, mechanistically unclear at the moment but are worth further exploration.

Acknowledgments

The partial support of the U.S. Army Research Office through grants W911NF-12-1-0317 and W911NF-16-1-0093 are gratefully acknowledged. The insightful comments from Professor K. Ravi-Chandar of the University of Texas at Austin are greatly appreciated.

Appendix-A

Experimental repeatability

Multiple experiments were conducted for all the four configurations to ensure repeatability in terms of dynamic fracture behavior as well as the measured fracture parameters. Fig. A1(a)-(d) shows photographs of two fractured samples each for all the four configurations. A high degree of reproducibility in terms of crack paths during the fracture event is clearly evident from these photographs. (The repeatability of fracture parameters for PMMA bilayers has already been reported in authors' previous study (Sundaram and Tippur, 2016).) Despite the highly transient nature of the problem, and potential variations in material and interface characteristics, a rather high degree of reproducibility of results is evident.

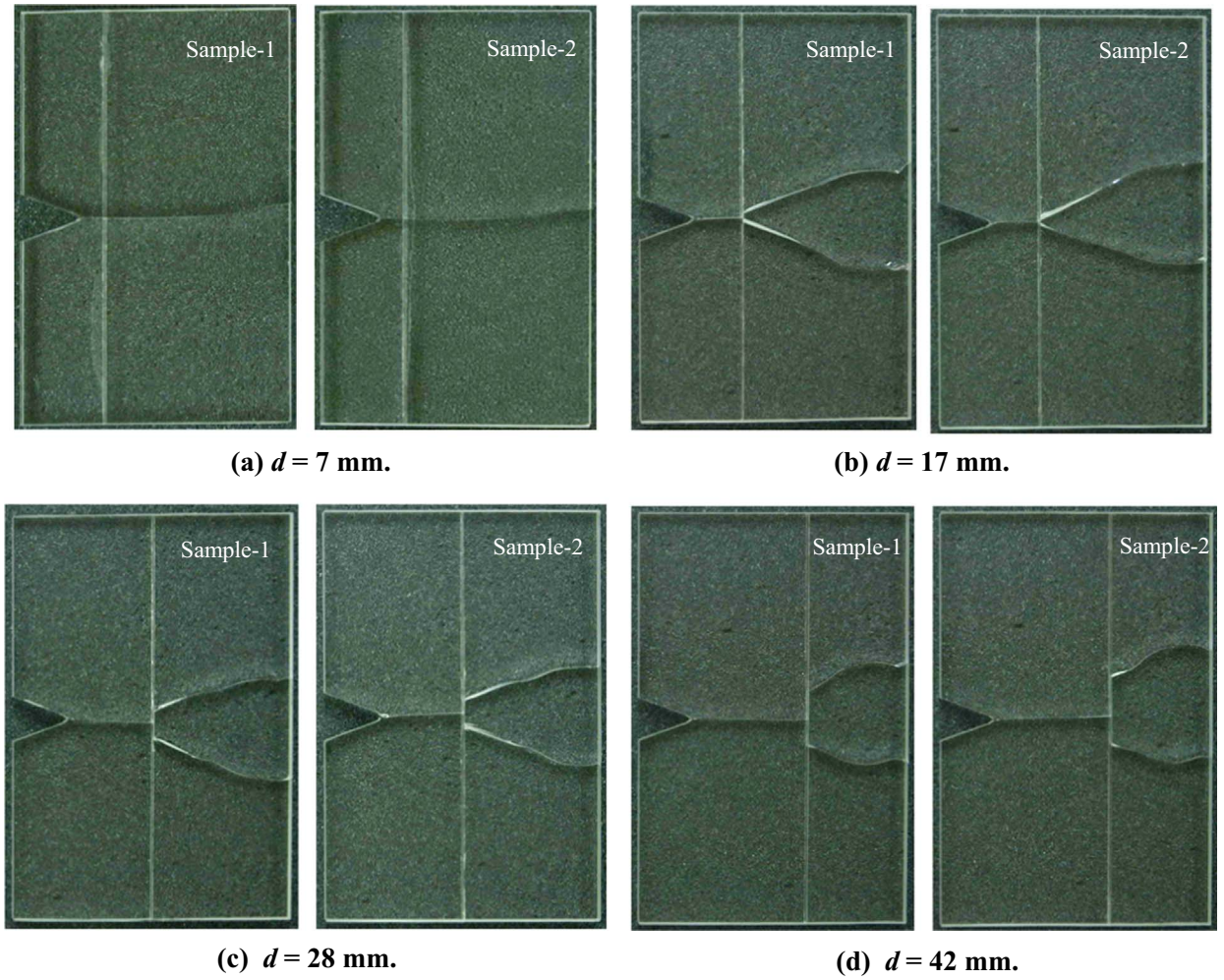

Fig. A1. Multiple fractured samples of each configuration showing experimental repeatability in terms of crack path and fracture behavior.

Appendix-B

Mode-I Interface fracture toughness: Interface thickness

The interface was characterized by measuring quasi-static crack initiation toughness using 3-point bend tests on edge cracked samples. Two rectangular 70 mm × 15 mm × 8.6 mm PMMA blocks (see Fig. B1(a)) were adhesively bonded along 8.6 mm × 15 mm faces using the acrylic adhesive Weldon 16. Metal shims of known thickness were used between the bonding surfaces to precisely control the bond thickness. Specimens with various bond layer thicknesses from 25 μm to 1.3 mm were prepared. A 3 mm long disbond was introduced along the interface of each sample during preparation. The

specimens were loaded symmetrically in displacement-control mode (cross-head speed 0.005 mm/sec, span = 120 mm). The applied load history up to fracture was recorded. Representative load-deflection plots for two select interface thicknesses, both showing abrupt failure, are shown in Fig. B1(b). The peak load was used to determine the interface crack initiation toughness of different interface thicknesses and is shown in Fig. B1(c). As the interface thickness increased, the crack initiation toughness decreased and all the values were lower than that of virgin PMMA ($= 1.31 \pm 0.07$ MPa$\sqrt{\text{m}}$; dotted-line in Fig. B1(c)). The crack initiation toughness of 100 μm interface considered in this work was 0.68 MPa$\sqrt{\text{m}}$ or ~52% of virgin PMMA.

Mixed-mode Interface fracture toughness of 100 μm interface

The mixed-mode fracture toughness of 100 μm thick interface was characterized using asymmetric four-point bending tests (Xu and Tippur, 1995; O'Dowd et al., 1992). The loading configuration used is shown in Fig. B2(a). The specimens were harvested by machining rectangular strips of width, $W = 16$ mm (and 100 mm span) from the fractured bilayer specimens used for performing dynamic crack growth experiments. A 4 mm long notch (a) was machined along the interface using a diamond saw to form SENB specimens. A razor blade was used to sharpen the interface notch tip prior to testing. An Instron 4465 universal testing machine was used for loading the specimen in the displacement-control mode (cross-head

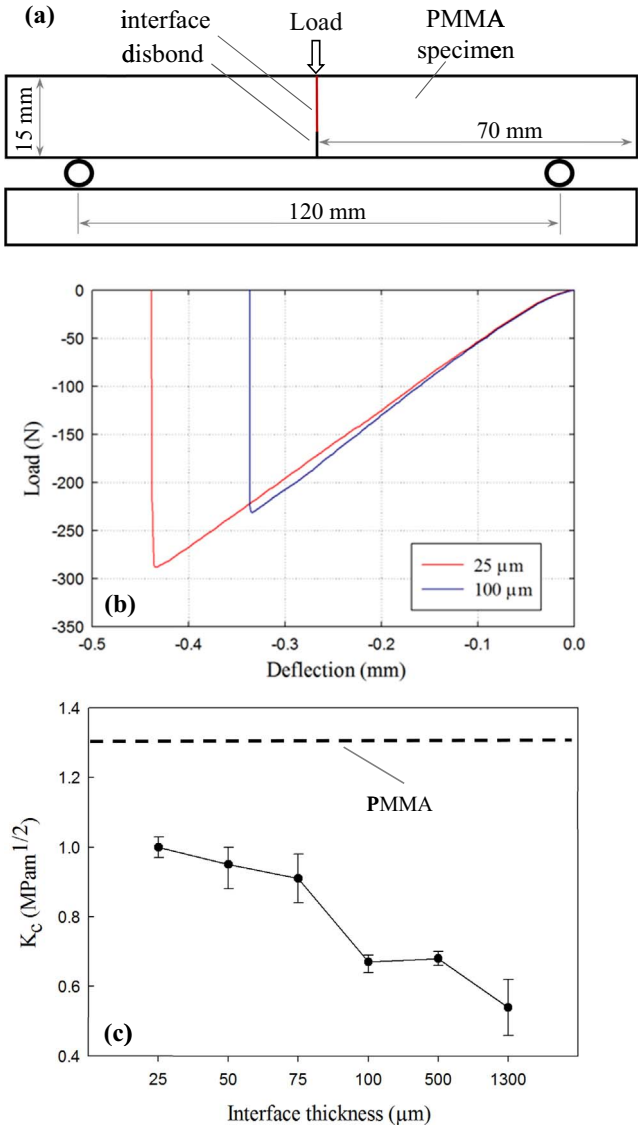

Fig. B1. (a) Photograph of the experimental setup for the interface characterization. (b) Measured load-deflection response for fracture specimens with 25 μm and 100 μm interface thicknesses. (c) Variation of crack initiation toughness with interface thickness. (Note that all interfaces have lower crack initiation toughness than virgin PMMA) (Sundaram and Tippur, 2016).

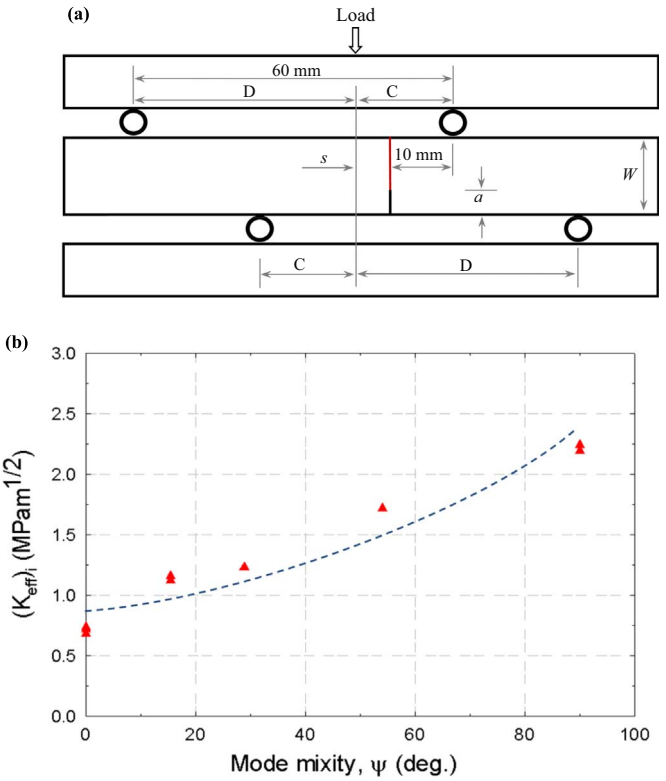

Fig. B2. Critical crack initiation toughness of 100 μm interface at different mode-mixities: (a) Asymmetric four-point-bend geometry and loading configuration ($W=16$ mm, $a=4$ mm), (b) Effective SIF at crack initiation vs. mode-mixity; dotted-line is a trend line.

speed=0.05 mm/sec). Multiple tests were carried out with length parameters C and D such that $(C+D)=60$ mm. From the failure load, the critical SIFs and mode-mixities were evaluated using (O'Dowd et al., 1992),

$$K_I = -\frac{P}{BW}\left[\frac{C-D}{C+D}\right]\left(\left(\frac{6s}{W}\right)f_1\right)\sqrt{a},\ K_{II} = -\frac{P}{BW}\left[\frac{C-D}{C+D}\right]f_2\sqrt{a},\ \text{and } \psi = \tan^{-1}\left(\left(\frac{f_2}{f_1}\right)\left(\frac{W}{6s}\right)\right) \tag{8}$$

where, P is the failure load and other variables in the above equation are described in the Fig. B2(a). Various values of s (0 mm, 2 mm, 5 mm and 10 mm) were used to achieve different mode-mixities. The geometric correction factors f_1 (=1.29) and f_2 (=1.86) were obtained from the plots reported in O'Dowd et al., (1992). The variation of K_{eff} with mode-mixity is shown in Fig. B2(b). Data points for zero mode-mixity obtained from mode-I tests on 100 μm thick interface from Fig. B1(c) are included in this plot. Evidently, the critical values of K_{eff} increase significantly ($\sim$0.68 MPa$\sqrt{\text{m}}$ for mode-I to $\sim$2.20 MPa$\sqrt{\text{m}}$ under mode-II conditions) and monotonically with mode-mixity.

Interface tensile strength

To measure the quasi-static tensile strength of the interface, tension tests were carried out. The experimental setup is shown in Fig. B3(inset). The specimen was prepared by bonding two PMMA sheets using the acrylic adhesive Weldon 16 with an interface thickness of 100 μm, the same thickness used to prepare bilayer fracture specimens in this study. The glued sheets were machined to final tension specimen (dog-bone) geometry, as shown. An Instron 4465 universal testing machine was used for loading the specimen in the displacement-control mode (cross-head speed=0.05 mm/sec). Multiple tests were carried out. The load-deflection plot obtained for two such experiments are shown in Fig. B3. From the failure load and area of cross-section (8.6 mm × 5 mm), the tensile strength of the interface was evaluated as 23 ± 0.3 MPa.

Interface shear strength

To measure the shear strength of the interface, asymmetric four-point bending shear tests (Xu and Tippur, 1995) were carried out. The loading configuration is shown in Fig. B4(a). Again, the specimen was prepared by bonding two PMMA sheets using the acrylic adhesive Weldon 16 with an interface thickness of 100 μm. The glued sheets were machined to the final specimen geometry and dimensions, as shown. An Instron 4465 universal testing machine was used for loading the

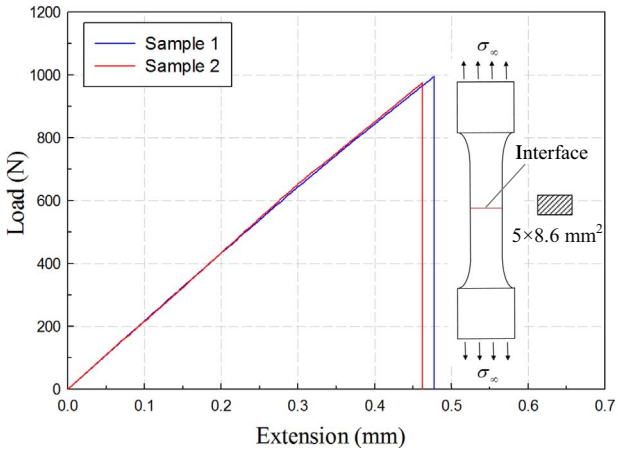

Fig. B3. Load-deflection plots for two tension tests (gage Section = 5 mm × 8.6 mm). Inset shows the dog-bone specimen geometry with interface.

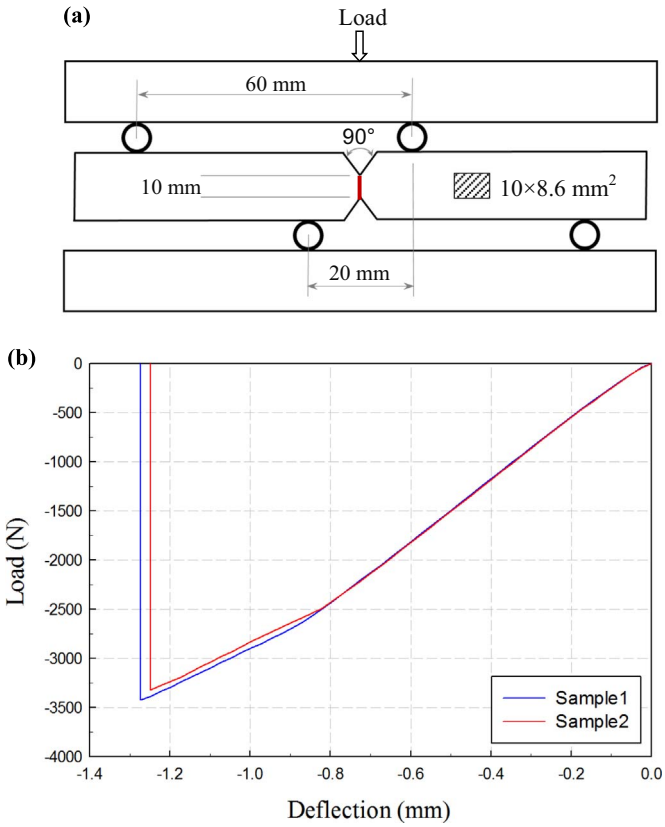

Fig. B4. Asymmetric four-point-bend tests: (a) Loading configuration and geometry, (b) Representative load-deflection plots.

specimen in the displacement-control mode (cross-head speed = 0.05 mm/sec). Multiple tests were carried out. The load-deflection plot obtained for two such experiments are shown in Fig. B4(b). From the failure load and area of cross-section (8.6 mm × 10 mm), the shear strength was evaluated. The quasi-static shear strength was found to be 26 ± 0.5 MPa.

References

Chalivendra, V.B., Rosakis, A.J., 2008. Interaction of dynamic mode-I crack with inclined interfaces. Eng. Fract. Mech. 75 (8), 2385–2397.
Coker, D., Rosakis, A.J., 2001. Experimental observation of intersonic crack growth in symmetrically loaded unidirectional composite plates. Philos. Mag. A 81 (3), 571–595.

Cook, J., Gordon, J.E., 1964. A mechanism for the control of crack propogation in all-brittle systems. Proc. R. Soc. A: Math. Phys. Eng. Sci. 282 (1391), 508–520.
Dally, J.W., 1979. Dynamic photoelastic studies of fracture. Exp. Mech. 19 (10), 349–361.
Freund, L.B., 1998. Dynamic Fracture Mechanics. Cambridge University Press, Cambridge New york Melbourne.
Gupta, V., Argon, A.S., Suo, A., 1992. Crack deflection at interface between two orthotropic materials. J. Appl. Mech. 59 (S2), S79–S87.
He, M.Y., Hutchinson, J.W., 1989. Crack deflection at an interface between dissimilar elastic materials. Int. J. Solids Struct. 25 (9), 1053–1067.
Hu, W., Wang, Y., Yu, J., Yen, C.F., Bobaru, F., 2013. Impact damage on a thin glass plate with a thin polymer backing. Int. J. Impact Eng. 62, 152–165.
Jajam, K.C., Tippur, H.V., 2012. Role of inclusion stiffness and interfacial strength on dynamic matrix crack growth: an experimental study. Int. J. Solids Struct. 49 (12), 1127–1146.
Lambros, J., Rosakis, A.J., 1995. Shear dominated transonic crack growth in bimaterial-I: experimental observation. J. Mech. Phys. Solids 43 (2), 169–188.
Leguillion, D., Lacroix, C., Martin, E., 2000. Interface debonding ahead of a primary crack. J. Mech. Phys. Solids 48 (10), 2137–2161.
Liu, L.G., Ou, Z.C., Duan, Z.P., Pi, A.G., Huang, F.L., 2011. Strain-rate effects on deflection/penetration of crack terminating perpendicular to bimaterial interface under dynamic loadings. Int. J. Fract. 167 (2), 135–145.
Maleski, M.J., Kirugulige, M.S., Tippur, H.V., 2004. A method for measuring mode-I crack tip constraint under static and dynamic loading conditions. Exp. Mech. 44 (5), 522–532.
O'Dowd, N.P., Shih, C.F., Stout, M.G., 1992. Test geometries for measuring interfacial fracture toughness. Int. J. Solids Struct. 29 (5), 571–589.
Paramgiani, J.P., Thouless, M.D., 2006. The role of toughness and cohesive strength on crack deflection at interfaces. J. Mech. Phys. Solids 54 (2), 226–287.
Park, H., Chen, W., 2011. Experimental investigation on dynamic crack propagating perpendicular through interface in glass. J. Appl. Mech. 78 (5), 051013.
Periasamy, C., Tippur, H.V., 2013. Measurement of orthogonal stress gradients due to impact load on a transparent sheet using digital gradient sensing method. Exp. Mech. 53 (1), 97–111.
Prautzsch, H., Boehm, W., Paluszny, M., 2002. Bezier and B-Spline Techniques. Springer-Verlag, Berlin Heidelberg, New York.
Ravi-Chandar, K., Knauss, W.G., 1984. An experimental investigation into dynamic fracture: III. On steady-state crack propogation and crack branching. Int. J. Fract. 26 (2), 141–154.
Rosakis, A.J., Samudrala, O., Singh, R.P., Shukla, A., 1998. Intersonic crack propogation in bimaterial systems. J. Mech. Phys. Solids 46 (10), 1789–1813.
Siegmund, T., Fleck, N.A., Needleman, A., 1997. Dynamic crack growth across interface. Int. J. Fract. 85 (4), 381–402.
Sundaram, B.M., Tippur, H.V., 2016. Dynamic crack growth normal to an interface in bi-layered materials: an experimental study using digital gradient sensing technique. Exp. Mech. 56, 37–57.
Sundaram, B.M.,Tippur, H.V., Dynamic mixed-mode fracture study of PMMA and polycarbonate using digital gradient sensing, in preparation.
Timmel, M., Kolling, S., Osterrieder, P., DuBois, P.A., 2007. A finite element model for impact simulation with laminated glass. Int. J. Impact Eng. 34 (8), 1465–1478.
Tippur, H.V., Rosakis, A.J., 1991. Quasi-static and dynamic crack growth along bimaterial interfaces: a note on crack tip field measurements using coherent gradient sensing. Exp. Mech. 31 (3), 243–251.
Washabagh, P.G., Knauss, W.G., 1994. A reconciliation of dynamic crack growth velocity and Rayleigh wave speed in isotropic brittle solids. Int. J. Fract. 65 (2), 97–114.
Xia, S., Ponson, L., Ravichandran, G., 2012. Toughening and symmetry in peeling of heterogeneous adhesives. Phys. Rev. Lett. 108 (19), 196101.
Xu, L.R., Hung, Y.Y., Rosakis, A.J., 2003. Dynamic crack deflection and penetration at interface in homogeneous materials: experimental studies and model predictions. J. Mech. Phys. Solids 51 (3), 461–486.
Xu, L., Tippur, H.V., 1995. Fracture parameters for interfacial cracks: an experimental-finite element study of crack tip fields and crack initiation toughness. Int. J. Fract. 71 (4), 345–363.
Xu, L.R., Wang, P., 2006. Dynamic fracture mechanics of failure mode transitions along weakened interfaces in elastic solids. Eng. Fract. Mech. 73 (12), 1597–1614.